Which impeller should be chosen for efficient solid-liquid mixing in the laminar regime?

Bastien Delacroix[a], Louis Fradette[a], François Bertrand[a,*], Bruno Blais[a,*]

[a]*Research Unit for Industrial Flows Processes (URPEI), Department of Chemical Engineering, École Polytechnique de Montréal, PO Box 6079, Stn Centre-Ville, Montréal, QC, Canada, H3C 3A7*

Abstract

The vast majority of solid-liquid mixing studies have focused on high Reynolds number applications with configurations and impeller geometries adapted to this type of regime. However, the mixing of particles in a viscous fluid is an essential element of many contemporary industries. We used the CFD-DEM model previously developed in our group to investigate solid-liquid mixing with close-clearance impellers in the laminar regime of operation. We compared different geometries that is, the double helical ribbon, anchor, Paravisc^{TM}, and Maxblend^{TM} impellers. We investigated the impact of fluid viscosity and compared the results with those obtained with the pitched blade turbine, a more commonly used impeller, based on power consumption for equivalent mixing states. This study highlights that the higher the viscosity of the fluid, the more interesting it is to use close-clearance impellers for their ability to generate a strong shear stress and a strong bulk flow in the entire vessel.

Keywords: CFD-DEM, non-inertial frame, solid-liquid mixing, laminar regime, close-clearance impeller

1. Introduction

Mixing is an essential operation for optimizing interactions between phases, homogenizing a system, or performing chemical transformations. This operation is at the core of many physical processes, including adsorption, desorption, dissolution, and catalyzed reactions

*Corresponding authors

Email addresses: francois.bertrand@polymtl.ca (François Bertrand), bruno.blais@polymtl.ca (Bruno Blais)

[1]. This is why mixing plays a key role in numerous industrial sectors, including food processing, pulp and paper, pharmaceuticals, water treatment, and petrochemicals [2]. Since the pioneering work of Kneule (1954) [3], Hirkerson and Miller (1953) [4], and Zwietering (1958) [5], our understanding of solid-liquid mixing has evolved constantly over the last 60 years. Suspending particles in a fluid to ensure an optimal contact area in order to increase the mass transfer between the two phases is one of the main challenge of this process [6]. One of the most important parameters used to characterize a solid-liquid mixing operation is thus the minimum agitation speed for complete suspension (N_{js}), which has been defined as the minimum agitation speed at which all the particles are not in contact with the bottom of the vessel for more than 2s [5]. The complexity of multiphase physical phenomena and the multitude of parameters involved in such operations make it a challenging area of research.

Most research on solid-liquid mixing has been devoted to the study of the turbulent regime. All the correlations developed to estimate N_{js} have focused on this regime, as shown by the work of Nienow *et al.* in 1968 [7], Baldi *et al.* in 1978 [8], Armenante et *al.* in 1998 [9], Ayranci *et al.* in 2013 [10], Tamburini *et al.* in 2014, [11], Grenville *et al.* in 2016 [12] and, more recently, Choong *et al.* [13]. However, the limitations of Zwietering correlation for determining N_{js} [14, 15, 16] show that the mixing dynamics are completely different in the laminar regime.

Moreover, these studies led in the turbulent regime focused on the impact of geometrical configurations such as the diameter of the impeller [11, 12], the off-bottom clearance [17, 18, 19], and the influence of the baffle [20]. In addition, the same impeller geometries were often used, such as the pitched blade turbine (PBT) or the Rushton turbine [21, 22, 23, 24].

When operating in the laminar regime, it is preferable to use close-clearance impellers [25, 26]. Numerous single-phase studies with viscous fluids have been carried out with close-clearance impellers, including the anchor [27, 28, 29], ribbon [**?** **?**], Paravisc^{TM} [30, 31], and Maxblend^{TM} turbine [32, 33]. To our knowledge, only two experimental studies [34, 35] and one numerical study [36] have investigated the performance of close-clearance impellers

in solid-liquid mixing applications.

This can be explained by the challenge posed by numerically modeling mixing systems with close-clearance impellers. Modeling rotating geometries, such as impellers is commonly done using methods such as the multiple reference frame [37, 38], sliding mesh [39, 23, 24, 40, 41] or the immersed boundary [42]. In a previous study we showed that these methods cannot be used straightforwardly for close-clearance impellers, which is why we developed a new CFD-DEM model based on a rotating frame of reference approach that makes it possible to study any axially symmetrical impeller [43].

The main objective of the present work is to compare the solid-liquid mixing efficiency in the laminar regime of four different close-clearance impellers with the more commonly used PBT impeller. We studied the anchor, double helical ribbon, Paravisc and, Maxblend close-clearance impellers. The present paper is divided into four main parts. First, we present the numerical model used in the study and the specifics required to cope with the extreme complexity of the systems under study. Then, we introduce the different mixing systems and a single-phase approach is used to analyze the power performance of each impeller configuration. The third part is devoted to the solid-liquid mixing aspect with an analysis of suspension dynamics using parameters such as N_{js}, cloud height, and solid distribution. Lastly, we describe the influence of pure-fluid viscosity on the behavior of each impeller.

2. Model description

We used a previously developed unresolved CFD-DEM model in a rotating frame of reference [44, 43]. The model is based on the CFDEM platform [45], which combines two open source software packages, i.e, LIGGGHTS [46] for granular dynamics using the discrete element method (DEM) and OpenFOAM [47] for the computational fluid dynamics (CFD). The CFD part is based on a cell-centered finite volume approach. In this section, we briefly recall the essential elements of this model. For more details the reader is referred to papers specifically devoted to the development of this model [43, 48].

2.1. Equations of motion for the solid phase - Discrete Element Method (DEM)

DEM is a Lagrangian approach for modeling granular flows where each particle is considered as a discrete entity. The method integrates Newton's second law of motion to calculate the velocity and position of each particle at every time step of the simulation.

It specifically deals with collisions by allowing particles to overlap. The overlaps are detected by comparing the distance of two particles to the sum of their radii. If two particles overlap, a spring and dashpot model is used to compute a contact force that is decomposed into elastic and dissipative components. Each of these components is then divided into a tangential and a normal term.

Based on Newton's second law of motion, the governing equations for the translational ($\boldsymbol{u}_{p,i}$) and rotational ($\boldsymbol{\omega}_{p,i}$) motions of particle i in a non-inertial frame of reference can be written as [46, 49, 50, 51]:

$$m_i \frac{d\boldsymbol{u}_{p,i}}{dt} = \sum_j \boldsymbol{f}_{c,ij} + \sum_k \boldsymbol{f}_{lr,ik} + \boldsymbol{f}_{pf,i} + \boldsymbol{f}_{g,i} - \underbrace{2m_i \boldsymbol{\Omega} \times \boldsymbol{u}_{p,i}}_{\boldsymbol{F}_{Coriolis}} - \underbrace{m_i \boldsymbol{\Omega} \times (\boldsymbol{\Omega} \times \boldsymbol{q}_{p,i})}_{\boldsymbol{F}_{Centrifugal}} \tag{1}$$

$$I_i \frac{d\boldsymbol{\omega}_{p,i}}{dt} = \sum_j (\boldsymbol{M}_{t,ij} + \boldsymbol{M}_{r,ij}) - \underbrace{I(\boldsymbol{\Omega} \times \boldsymbol{\omega}_{p,i})}_{\boldsymbol{T}_{Coriolis}} \tag{2}$$

where m_i is the mass of particle i, $\boldsymbol{\Omega}$ is the rotation vector of the frame of reference, $\boldsymbol{q}_{p,i}$ and $\boldsymbol{u}_{p,i}$ are the position (from the projection point on the axis of rotation: $\boldsymbol{q}_{p,i} \cdot \boldsymbol{\Omega} = 0$) and velocity vectors of a particle i, I_i is the moment of inertia of particle i, $\boldsymbol{\omega}_{p,i}$ is the angular velocity of particle i, $\boldsymbol{f}_{c,ij}$ is the contact forces between particles i and j, $\boldsymbol{f}_{lr,ik}$ is the non-contact (long-range) forces between particles i and k, $\boldsymbol{f}_{pf,i}$ is the particle-fluid interaction forces, $\boldsymbol{f}_{g,i}$ is the gravitational force ($\boldsymbol{f}_{g,i} = m_i \boldsymbol{g}$), and $\boldsymbol{M}_{t,ij}$ and $\boldsymbol{M}_{r,ij}$ are the tangential and rolling friction torques acting on particle i due to its contact with particle j. In the present work, non-contact forces such as electrostatic or Van Der Waals forces in (1) and Coriolis torque in (2) were not taken into account due to the size and nature of the particles [44].

The contact forces between two particles are split into normal ($\boldsymbol{f}_{cn,ij}$) and tangential

($\boldsymbol{f}_{ct,ij}$) [52] components:

$$\boldsymbol{f}_{c,ij} = \boldsymbol{f}_{cn,ij} + \boldsymbol{f}_{ct,ij} = -k_{n,ij}\boldsymbol{\delta}_{n,ij} - \gamma_{n,ij}\dot{\boldsymbol{\delta}}_{n,ij} - k_{t,ij}\boldsymbol{\delta}_{t,ij} - \gamma_{t,ij}\dot{\boldsymbol{\delta}}_{t,ij} \tag{3}$$

where $k_{n,ij}$ and $k_{t,ij}$ are the normal and tangential stiffness coefficients, $\gamma_{n,ij}$ and $\gamma_{t,ij}$ are the normal and tangential damping coefficients, $\boldsymbol{\delta}_{n,ij}$ and $\boldsymbol{\delta}_{t,ij}$ are the normal and tangential overlaps, and $\dot{\boldsymbol{\delta}}_{n,ij}$ and $\dot{\boldsymbol{\delta}}_{t,ij}$ are their derivatives with respect to time.

In the present work, we used a model proposed by Tsuji *et al.* [53] that is based on the Hertz theory [54] for normal forces. We used the Mindlin model [55] for tangential forces. These models were combined to couple the stiffness and damping coefficients to Young's modulus of the material (Y), Poisson's ratio (ν), and the coefficient of restitution (e_r) using the equations given in Table 1. Tangential overlap $\boldsymbol{\delta}_{t,ij}$ was truncated using Coulomb's law to ensure that: $\boldsymbol{f}_{ct,ij} \leq -\mu_{s,ij}\left|\boldsymbol{f}_{cn,ij}\right| \frac{\boldsymbol{\delta}_{t,ij}}{|\boldsymbol{\delta}_{t,ij}|}$.

Parameter	Equation
Normal stiffness	$k_{n,ij} = \frac{4}{3}Y^*_{ij}\sqrt{R^*_{ij}\delta_{n,ij}}$
Tangential stiffness	$k_{t,ij} = 8G^*_{ij}\sqrt{R^*_{ij}\delta_{n,ij}}$
Normal damping	$\gamma_{n,ij} = -2\sqrt{\frac{5}{6}}\frac{\ln(e_r)}{\sqrt{\ln^2(e_r)+\pi^2}}\sqrt{\frac{2}{3}k_n m^*_{ij}}$
Tangential damping	$\gamma_{t,ij} = -2\sqrt{\frac{5}{6}}\frac{\ln(e_r)}{\sqrt{\ln^2(e_r)+\pi^2}}\sqrt{k_t m^*_{ij}}$
Coulomb friction force	$\boldsymbol{f}_{ct,ij} \leq -\mu_{s,ij}\left\|\boldsymbol{f}_{cn,ij}\right\| \frac{\boldsymbol{\delta}_{t,ij}}{\|\boldsymbol{\delta}_{t,ij}\|}$
Torque by tangential force	$\boldsymbol{M}_{t,ij} = \boldsymbol{r}_i \times (\boldsymbol{f}_{ct,ij})$
Rolling friction torque	$\boldsymbol{M}_{r,ij} = -\mu_{r,ij}\left\|\boldsymbol{f}_{cn,ij}\right\| \frac{\boldsymbol{\omega}_{p,ij}}{\|\boldsymbol{\omega}_{p,ij}\|} R^*_{ij}$
Equivalent mass	$\frac{1}{m^*_{ij}} = \frac{1}{m_i} + \frac{1}{m_j}$
Equivalent radius	$\frac{1}{R^*_{ij}} = \frac{1}{R_i} + \frac{1}{R_j}$
Equivalent Young's modulus	$\frac{1}{Y^*_{ij}} = \frac{\left(1-\nu_i^2\right)}{Y_i} + \frac{\left(1-\nu_j^2\right)}{Y_j}$
Equivalent shear modulus	$\frac{1}{G^*_{ij}} = \frac{2(2+\nu_i)(1-\nu_i)}{Y_i} + \frac{2(2+\nu_j)(1-\nu_j)}{Y_j}$
Sliding friction coefficient	$\mu_{s,ij}$
Rolling friction coefficient	$\mu_{r,ij}$
Distance to contact point for particle i	$\boldsymbol{r}_i$
Radius of particle i	R_i

Table 1: Equations for the DEM model adapted from [48]

2.2. Equations of motion for the liquid phase (CFD)

Volume-averaged Navier–Stokes equations (VANS) are commonly used in CFD-DEM. In the particular context of rotating frames of reference, we previously showed that these equations lead to a destabilization of CFD-DEM simulations at t=0 [43]. The fluid model was thus based on the Navier-Stokes equations (Eq.4 and Eq.5).

$$\frac{\partial}{\partial t}(\rho_f) + \nabla \cdot (\rho_f \boldsymbol{u}_f) = 0 \tag{4}$$

$$\begin{aligned} \frac{\partial}{\partial t}(\rho_f \boldsymbol{u}_f) + \nabla \cdot (\rho_f \boldsymbol{u}_f \otimes \boldsymbol{u}_f) &= -\nabla P + \nabla \cdot \boldsymbol{\tau} + \boldsymbol{F}_g \\ \underbrace{-\frac{1}{\Delta V}\sum_{i}^{n_p}(\boldsymbol{f}_{pf,i} - \boldsymbol{f}_{\nabla p,i} - \boldsymbol{f}_{\nabla\cdot\boldsymbol{\tau},i})}_{\boldsymbol{F}_{pf}} &\underbrace{-2\rho_f \boldsymbol{\Omega} \times \boldsymbol{u}_f}_{\boldsymbol{F}_{Coriolis}} \underbrace{-\rho_f \boldsymbol{\Omega} \times (\boldsymbol{\Omega} \times \boldsymbol{q}_f)}_{\boldsymbol{F}_{Centrifugal}} \end{aligned} \tag{5}$$

$$\text{with} \quad \boldsymbol{f}_{pf,i} = \boldsymbol{f}_{drag,i} + \boldsymbol{f}_{Ar,i} + \boldsymbol{f}_{\nabla\cdot\boldsymbol{\tau},i} + \boldsymbol{f}_{\nabla p,i} + \sum \boldsymbol{f}_{add,i} \tag{6}$$

where $\boldsymbol{F}_g$ represent the gravity, $\boldsymbol{F}_{pf}$ the global momentum exchange between the fluid and the particles and $\boldsymbol{f}_{spf,i}$ represent the interaction force between the fluid and a particle i. This force includes the drag force $\boldsymbol{f}_{drag,i}$, the Archimedes force $\boldsymbol{f}_{Ar,i}$, the viscous forces $\boldsymbol{f}_{\nabla\cdot\boldsymbol{\tau},i}$, the pressure gradient force$\boldsymbol{f}_{\nabla p,i}$ and $\boldsymbol{f}_{add,i}$ that represent the different interaction forces between a particle and a fluid such as the virtual mass force, the Basset force and the lift forces (Magnus and Saffman) [56]. These latter forces are neglected in this work. The viscous stress tensor is defined as:

$$\boldsymbol{\tau} = \mu\left((\nabla \boldsymbol{u}_f) + (\nabla \boldsymbol{u}_f)^T - \frac{2}{3}(\nabla \cdot \boldsymbol{u}_f)\mathbb{I}\right) \tag{7}$$

where μ is the dynamic viscosity and $\mathbb{I}$ is the identity tensor. Lastly, the fluid solver used in the CFD-DEM model was based on a transient SRF-PISO solution algorithm that combines the single rotating frame approach with the PISO method [57].

2.3. CFD-DEM parameters

In this section, we describe the main CFD-DEM parameters making up the model.

2.3.1. Viscosity model

The presence of particles greatly influences the overall viscosity of the fluid at the particle scale [58]. However, with a numerical model based on an unresolved approach, the flow is solved at a larger scale than the particle scale. This is why, a viscosity model that takes the local particle fraction into account has to be used [48], in this case the Krieger-Dougherty model [59] (Eq.8).

$$\mu = \mu_0 \left(1 - \frac{\epsilon_p}{\epsilon_p^*}\right)^{-[\eta]\epsilon_p^*} \tag{8}$$

where $[\eta]$ the intrinsic viscosity parameter equal to 2.5 in the present study, ϵ_p^* is the maximum packing fraction taken equal to 0.64 for spherical particles [60], and μ_0 is the dynamic viscosity of the pure fluid.

2.3.2. Smoothing of the solid-liquid momentum exchange force

The divided approach was used to project the particles onto the fluid grid. Each particle is thus no longer seen as a single entity but as 27 parts of equal volume. Each part is projected onto the fluid grid. This increases the accuracy and robustness of the local void fraction and smoothes the coupling term between the fluid and the particles. However, this is insufficient to obtain good stabilization of the coupling scheme [48]. In the present study, we coupled an isotropic diffusive smoothing approach to the divided approach [61]. For a

quantity ζ, a parabolic filter was applied based on the following equation:

$$\frac{\partial \zeta}{\partial t} = \frac{\lambda^2}{\Delta t_{CFD}} \nabla^2(\zeta) \tag{9}$$

where λ is the characteristic smoothing length chosen to be equal to 3 particle diameters to ensure stability. For more details about the stakes of this smoothing process, we refer the reader to [43].

2.3.3. Coupling strategy

With the CFD-DEM method, the implicit strategy for the momentum exchange between the liquid and the solid phases is generally used ($\boldsymbol{F}_{pf} = K_{pf}(\boldsymbol{u}_p - \boldsymbol{u}_f)$ with $K_{pf} = \frac{|\boldsymbol{F}_{pf}|}{|\boldsymbol{u}_p - \boldsymbol{u}_f|}$). However, we showed in a previous paper that such coupling combined with rotating systems leads to fictitious forces created by the mesh topology [43]. We thus used an explicit coupling strategy whereby the coupling force $\boldsymbol{F}_{pf}$ was added directly to the fluid equation (Eq.5) without the use of the scalar K_{pf} [48].

To summarize, the solver used for the CFD-DEM simulations is a CFD-DEM-PISO-SRF solver based on the classical Navier-Stokes equations formulated in a rotating frame of reference with an explicit coupling between the liquid and solid phases.

2.3.4. Hydrodynamic force model

The study of the relative importance of each hydrodynamic force in a solid-liquid mixing operation is still an active area of research [22, 38, 62, 63, 64]. Based on previous studies conducted in the laminar regime [48], we considered the drag force as the predominant force in comparison with lift, Basset, and virtual mass forces. In addition, we have shown that the choice between different drag models that take into account the void fraction has no significant impact on the accuracy of the simulations [43]. In the present study we use the Di Felice drag model [65]. Due to the unresolved approach the particles are not discretized in the CFD part, it is thus necessary to add the pressure and viscous stress forces. All the expressions of these forces are detailed in Table 2.

Force	Equation
Pressure gradient	$-\frac{\pi}{6}d_p^3\nabla p$
Viscous force	$-\frac{\pi}{6}d_p^3\nabla\cdot\boldsymbol{\tau}$
Archimede's force	$-\rho_f V_p \boldsymbol{g}$
Drag force - Di Felice model	$\frac{1}{8}C_D\rho_f\pi d_p^2\epsilon_f^{2-X_i}\left\|\boldsymbol{u}_f-\boldsymbol{u}_p\right\|(\boldsymbol{u}_f-\boldsymbol{u}_p)$
	$X_i = 3.7 - 0.65\exp\left(\frac{-(1.5-log(R_{ep}))^2}{2}\right)$
	$C_D = \left(0.63+\frac{4.8}{\sqrt{R_{ep}}}\right)^2$
	$R_{ep} = \frac{d_p\epsilon_f\left\|\boldsymbol{u}_f-\boldsymbol{u}_p\right\|\rho_f}{\mu_f}$

Table 2: Expression of the force used in the CFD-DEM model.

2.3.5. Non-inertial frame: boundary and initial conditions

To conclude the description of the model, it is important to present the steps that are required to carry-out CFD-DEM simulations of solid-liquid mixing in a non-inertial frame of reference (i.e., a rotating frame). A simulation in a rotating frame of reference implies setting specific initial conditions on the liquid and the particles, and boundary conditions on the geometrical components. As the whole problem is reformulated in the impeller's frame of reference, the impeller is motionless during the simulations but the particles, the liquid and the vessel must be in motion from t=0. The different initial steps for the simulation of a mixing system are described and summarized in Figure 1.

3. Single-phase study of each impeller

Before discussing solid-liquid mixing, the different impellers used in our simulations are presented by examining their power consumption, often used in experimental studies as the starting point of the investigation.

3.1. Systems description

Of the different impeller geometries, four are close-clearance impellers ,i.e, the anchor, double helical ribbon, Paravisc, and Maxblend. The fifth is the commonly used PBT impeller. All the geometrical parameters used for the simulations are described in Table 3 and Figure 2. All the close-clearance impellers have the same characteristic dimensions to ensure

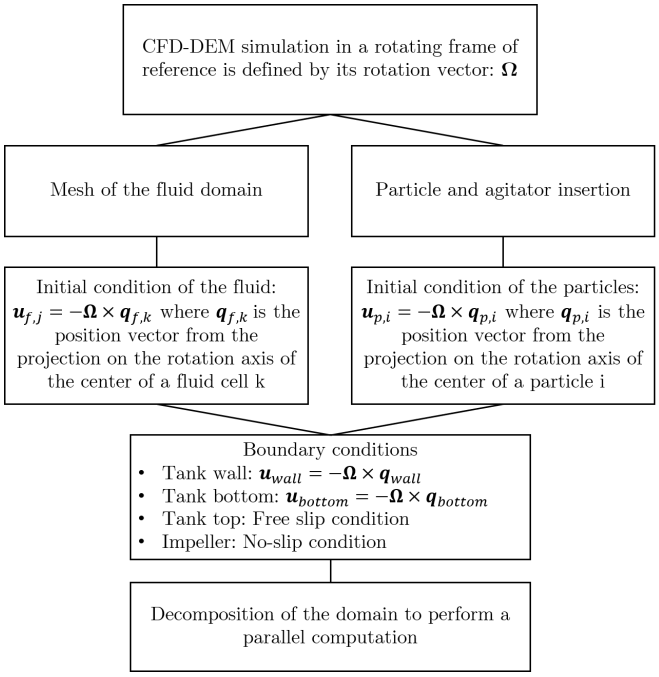

Figure 1: Initial and boundary conditions required for a CFD-DEM simulation in a rotating frame of reference (adapted from [43]).

a meaningful comparison. More precisely, as the diameter of all these impellers is the same, the Reynolds number $Re = \frac{\rho_f N D^2}{60\mu_f}$ used in the rest of the present study only depend on the agitation speed N (RPM). Note that this implies using an off-bottom clearance value for the Maxblend impeller that is higher than what can be found in the industry. This aspect will be discussed later in the study. For the PBT impeller, we use the same geometry as that used in [15, 43, 48].

Element	Symbols	Dimension	Ratio (dimension/T)
Tank diameter	T	36.5cm	1
Impeller diameter	D	33.3cm	0.9
Liquid height	H	36.5cm	1
Impeller height	S	28.7cm	0.8
Off-bottom clearance	C	4.56cm	0.12
Close clearance	E	1.6cm	0.04
Impeller thickness	e	0.4cm	0.01
Impeller width	W_b	3.6cm	0.1
Shaft diameter	T_i	2.54cm	0.07
PBT diameter	D_{pbt}	12.16cm	0.33
PBT blade height	S_{pbt}	2.4cm	0.07
PBT off-bottom clearance	C_{pbt}	9.1cm	0.25

Table 3: Geometrical parameters used for the simulations of mixing system with five different impellers.

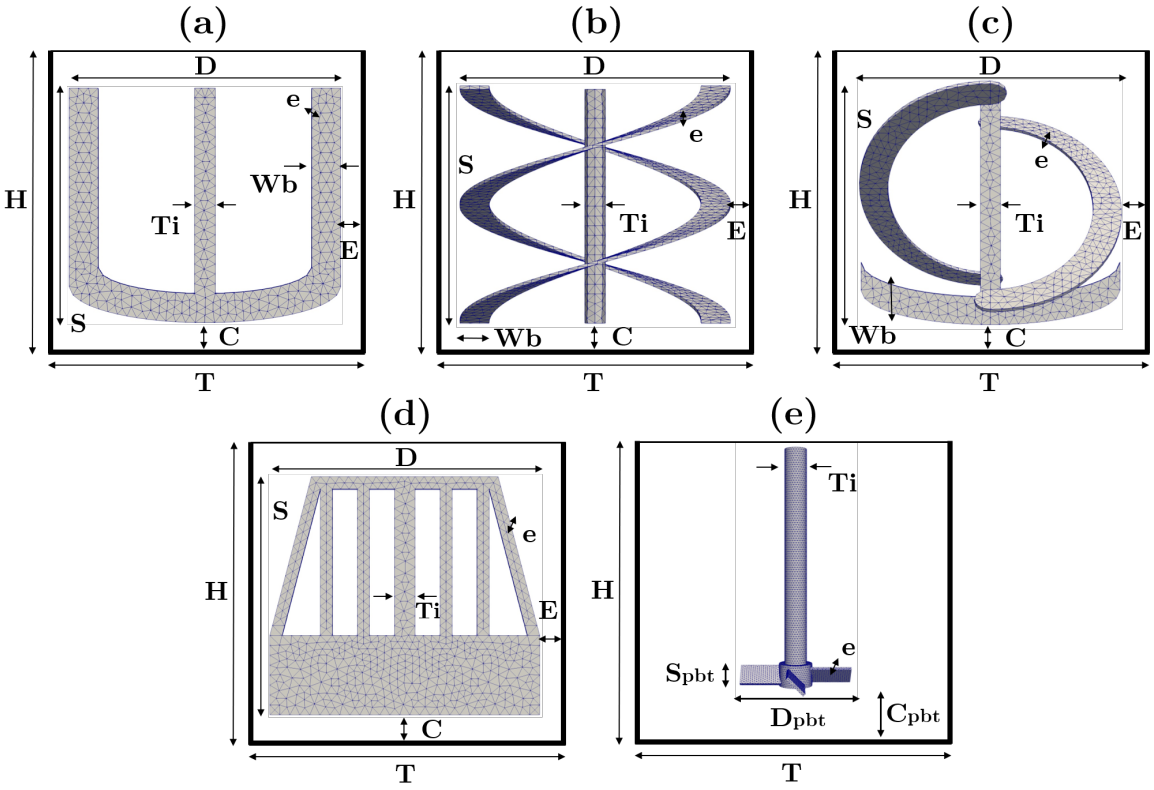

Figure 2: Geometry used in this study: (a) anchor, (b) double helical ribbon, (c) Paravisc, (d) Maxblend, and (e) PBT impellers.

All the single-phase simulations presented in this section were conducted using a Newtonian viscosity model with a constant dynamic viscosity of $\mu = 1Pa.s$. In addition, the rotation of the impeller in the Eulerian frame of reference was in the **clockwise** direction.

3.2. Mesh sensitivity analysis

The first step after presenting the different mixing system is to mesh the geometries. To carry out the mesh sensitivity analysis, an adimensional number commonly used in mixing is introduced. The power number is defined by the following equation:

$$Np = \frac{P}{\rho_f (N/60)^3 D^5} \tag{10}$$

where P is the power transmitted to the fluid by the impeller. For each system, we drew power curves N_p/Re for different meshes. The steady-state simulations were performed using the *SRFSimpleFoam* solver implemented in the OpenFOAM CFD software. This particular solver uses the single rotating frame (SRF) of reference approach combined with the SIMPLE resolution algorithm [66]. An illustration of the mesh used for the system studied is presented in Figure 3. The results of the mesh sensitivity analysis are shown in Table 4 (when the plateau is reached for $Re = 500$) and Figure 4. Based on these results, and to ensure a

Impeller	$1 - Np_1/Np_{ref}$	$1 - Np_2/Np_{ref}$	$1 - Np_3/Np_{ref}$	$1 - Np_4/Np_{ref}$
Anchor	**0.8%**	3.1%	8.6%	23%
Double ribbon	**1.1%**	3.2%	4.1%	5.1%
Paravisc	**0.9%**	4.9%	5%	5%
Maxblend	1.3%	**2.8%**	7.5%	32%
PBT	**0.4%**	2.8%	12%	13%

Table 4: Comparison of the N_p obtained when the plateau is reached for $Re = 500$ with the different meshes. Np_{ref} corresponds to the result obtained with the finest mesh and Np_i to the result obtained with increasingly coarse meshes. The selected mesh size for each system is highlighted in bold.

good compromise between computational time and accuracy of the results, we decided to use a mesh of $200k$ cells for the anchor system, a mesh of $200k$ cells for the ribbon system,

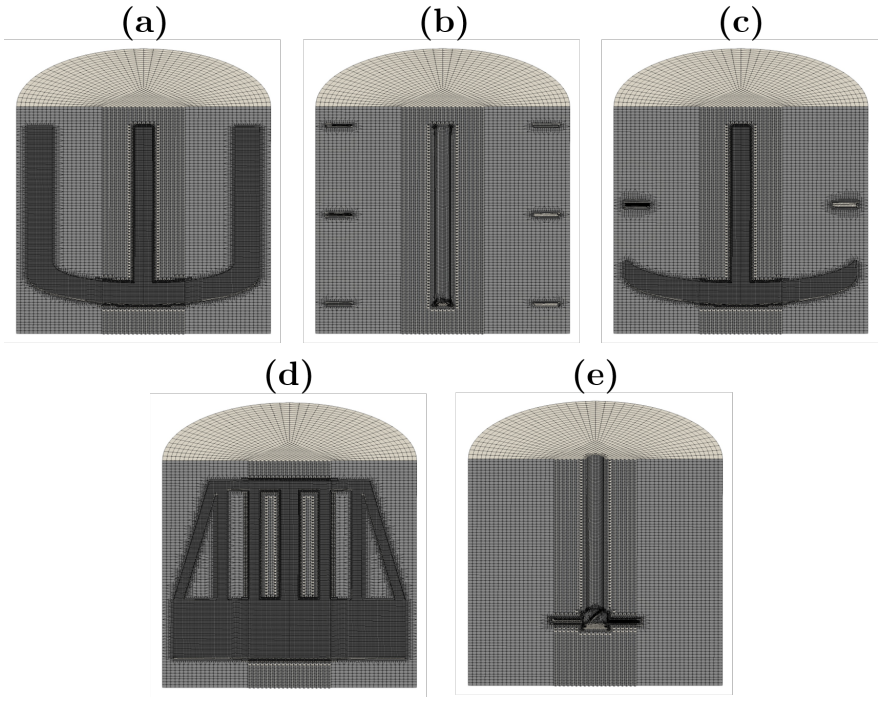

Figure 3: Illustration of the hexaedral mesh used for the (a) anchor, (b) double helical ribbon, (c) Paravisc, (d) Maxblend, and (e) PBT impellers.

a mesh of $220k$ cells for the Paravisc system, a mesh of $185k$ cells for the Maxblend system, and a mesh of $180k$ cells for the PBT system.

3.3. Velocity profile

In this section we study the flow of the liquid for the different configurations studied. This analysis is essential to understand the different mechanisms of particle suspension studied later. All the simulations were performed in the rotating Lagrangian frame of reference. However, the visualizations of the velocity profiles, are in the Eulerian frame of reference obtained using the following velocity composition relation:

$$\boldsymbol{v}_{eul} = \boldsymbol{v}_{lag} + \boldsymbol{\Omega} \times \boldsymbol{q}_{lag} \tag{11}$$

where $\boldsymbol{q}_{lag}$ is the position vector from the projection on the rotation axis of the center of a fluid cell in the Lagrangian frame. We compare the fluid velocity profile of the different mixing

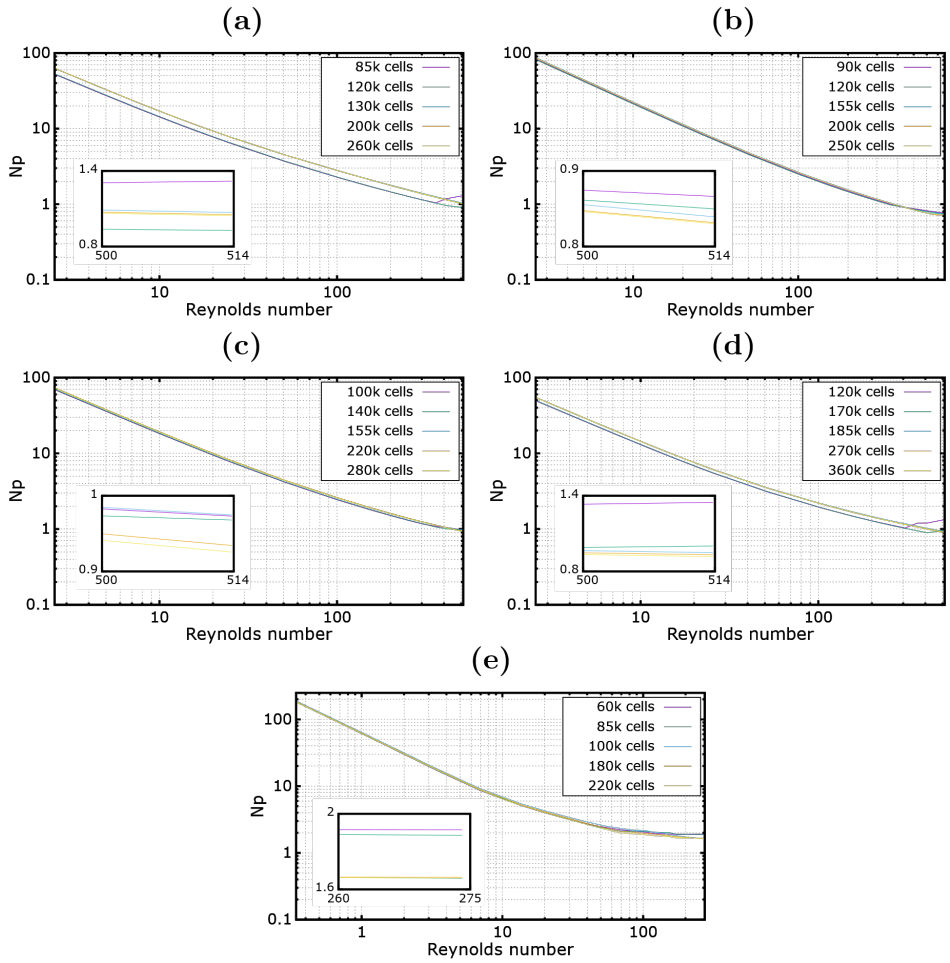

Figure 4: Mesh sensitivity analysis for the (a) anchor, (b) double helical ribbon, (c) Paravisc, (d) Maxblend, (e) PBT impellers. The zoom on each figure highlights the high Reynolds numbers when the plateau is reached. Steady-state simulations did not converge for high Reynolds numbers for the coarsest meshes in the case of the anchor and Maxblend impellers.

systems for a constant Reynolds number of $Re = 240$, which correspond to an agitation speed of 100RPM for the four close-clearance impellers and 700RPM for the PBT impeller. These profiles are shown in Figure 5.

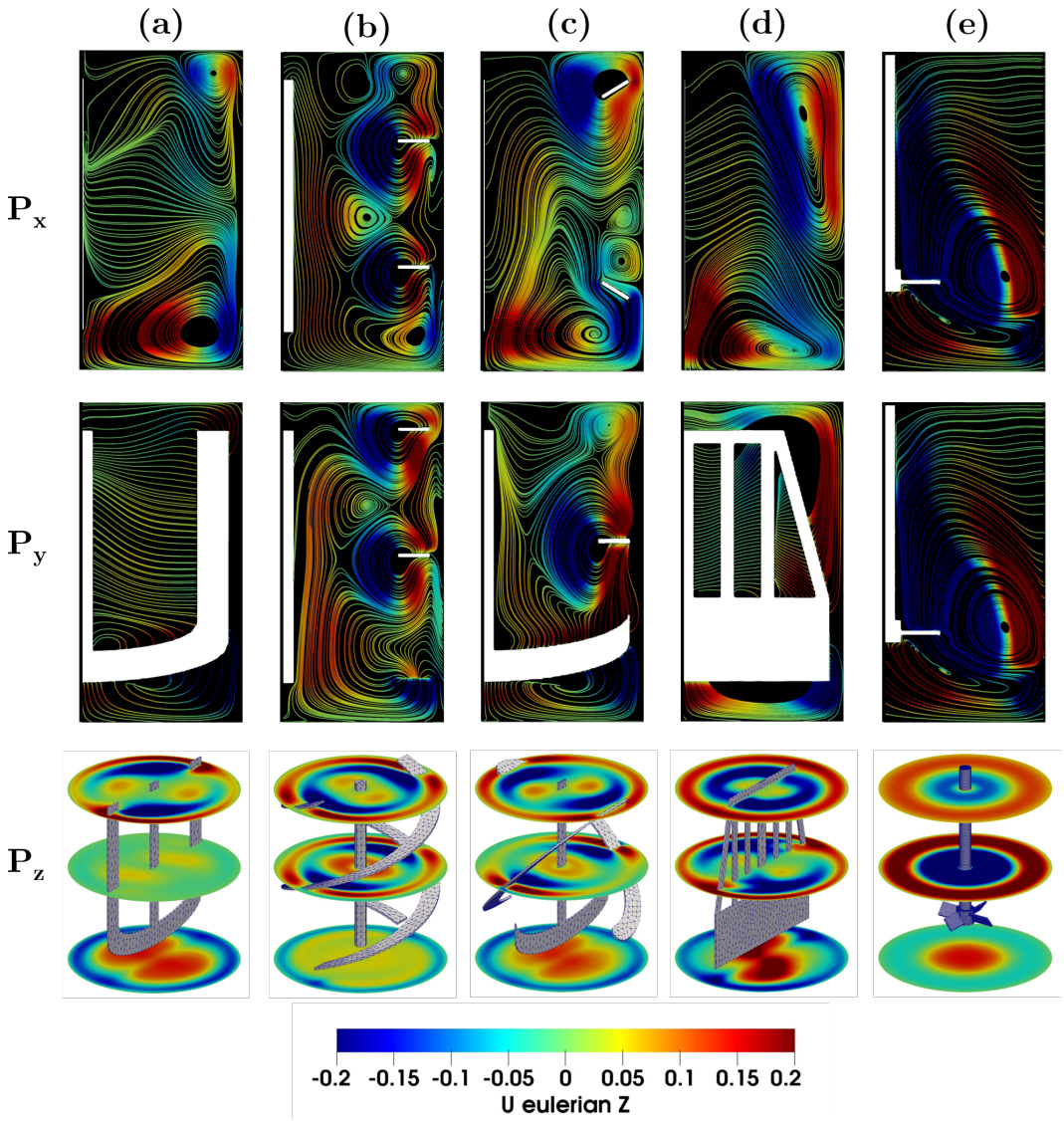

Figure 5: Fluid circulation in the x=0 plane P_x, y=0 plane P_y, and $z = 0.02$, $z = 0.18$, $z = 0.32$ planes P_z at steady-state with (a) anchor, (b) double helical ribbon, (c) Paravisc, (d) Maxblend, and (e) PBT impellers for a constant Reynolds number of $Re = 240RPM$. The color map represents the intensity of the axial flows while the lines represent the flow streamlines.

– For the anchor impeller (Figure 5 (a)) the flow generated is radial near the impeller. Two areas of significant recirculation, in opposite directions in the lower and upper

corners of the P_x plane, can be seen in Figure 5. These two zones imply that the radial flow splits into ascending and a descending streams along the wall, creating a stagnation of the flow. This is clearly visible in the middle P_z plane.

– For the ribbon impeller (Figure 5 (b)) the flow generated is relatively complex, with many recirculation zones. At the level of each ribbon, recirculation zones that encircle them can be seen. These recirculations generate further recirculations in the entire vessel as can be observed in the P_x plane. In addition, similar global behavior can be observed in the P_x, P_y, and P_z planes, i.e., an ascending flow along the shaft and the wall, and a descending flow between the two.

– For the Paravisc impeller (Figure 5 (c)), the flow is a combination of the streams observed for the other two configurations. The same recirculation zones encircling the ribbons can be observed. The same separation of the flow can be seen in the middle of the vessel, with an ascending part and a descending part (P_x plane). However, unlike to the anchor impeller the flow is not completely radial near the shaft (P_y plane). In addition, the intensity of the flow in the middle P_z plane is much greater with the Paravisc impeller.

– For the Maxblend impeller (Figure 5 (d)) the flow is characterized by two major recirculation zones that are clearly visible on the P_x plane. This is similar to what can be observed with the anchor impeller. However, contrary to the anchor impeller there is no splitting of the fluid flow. Indeed, continuous ascending and descending streams can be seen in the vessel. It is interesting to note that, in terms of magnitude, the flow generated by the Maxblend impeller is greater than for the other impellers (P_z planes).

– For the PBT impeller (Figure 5 (e)), as expected [15, 18], the flow is a combination of axial and radial components. It is axial (P_z planes) along the walls and directly under

the shaft while and radial close to the blades. This results in a large recirculation area at the blade tips (P_x and P_y planes).

These observations are in perfect agreement with previous single-phase studies carried out with similar geometries [15, 67, 68, 69, 70]. The main conclusion is that the axial component is the main component of the flow generated by all these impellers, but that the intensity of this flow varies with the type of impeller. In addition, numerous recirculation zones can be observed, which is very interesting because, according to Ibrahim *et al* [16], recirculation zones are the main mechanism for suspending particles in viscous fluids.

3.4. Power consumption

In this section, we discuss the power consumption of each impeller. The power consumption is a convenient parameter to compare very different mixing configurations. The power curves in Section 3.2 are used to calculate the Kp of each system, which is defined as the product of the Reynolds number and the power number (Figure 6).

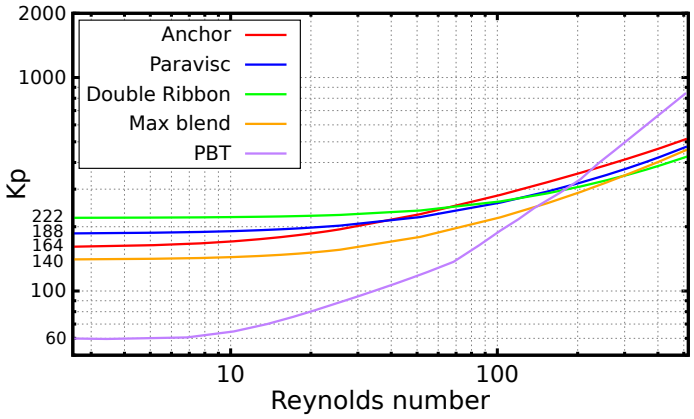

Figure 6: Evolution of $Kp = NpRe$ as a function of the Reynolds number for the five systems studied.

We obtain a constant Kp for a low Reynolds number, below Re=10 in most cases, as expected, for mixing in the creeping flow regime [6].

The energy performance of similar systems has already been studied, and some correlations have been developed to estimate the value of Kp. The work by Sawinsky *et al* [29] on

the anchor impeller system led to the following correlation:

$$K_{p,anchor} = 17 \left(\frac{2S + D}{D} \right) \left(\frac{D}{E} \right)^{0.45} \tag{12}$$

where E is the close-clearance and S is the impeller height.

For ribbon impellers, the study by Delaplace *et al* [71] led to the following correlation:

$$K_{p,ribbon} = 91 \cdot Nr^{0.79} \left(0.5 \left(\frac{T}{D} - 1 \right) \right)^{-0.31} \left(\frac{s}{D} \right)^{-0.37} \left(\frac{W_b}{D} \right)^{0.16} \left(\frac{S}{D} \right) \tag{13}$$

where Nr is the number of ribbons and s is the pitch that corresponds to the distance between two vertically aligned points on the same ribbon. In our case, $Nr = 2$ and $s = S$.

For the Paravisc system, other studies by Delaplace *et al* [72, 30] led to an adaptation of the previous correlation, which resulted in:

$$K_{p,paravisc} = 66 \cdot Nr^{0.84} \left(0.5 \left(\frac{T}{D} - 1 \right) \right)^{-0.29} \left(\frac{s}{D} \right)^{-0.44} \left(\frac{S}{D} \right) \tag{14}$$

In the case of our system with the Paravisc impeller, each ribbon makes only a half turn, and the bottom of each ribbon starts at the top of the anchor. Thus, the pitch (s) is $s = 2 \cdot (S - W_b)$.

The results obtained with these correlations and our numerical simulations are reported in Table 5.

	Anchor	Double helical ribbon	Paravisc
$K_{p,correlation}$	189	257	205
$K_{p,simulation}$	164	222	188

Table 5: Comparison of the K_p coefficients from the empirical correlations and those obtained with the numerical simulations.

A slight difference can be observed between the results. The previously described correlations were formulated for $E = C$ but, in our case, the off-bottom clearance C is higher.

The impellers are thus further from the lower wall, which reduces the shear stress generated in this zone. This explains why our numerical Kp values are lower those of the correlations for the close clearance impellers. Keeping in mind that Kp is the product of both Np and Re, it is extremely sensitive to both its constituents. Hence, a small difference as presented in the table above makes us confident in the adequacy of our simulations. Along the same line, we must also underline the fact that our comparison point is based on correlations having their own uncertainties.

3.5. Shear stress analysis

The onset of particle suspension in the laminar regime is controlled by an erosion mechanism that closely resembles shear-induced migration [15, 18, 48]. The shear stress τ, where $\boldsymbol{\tau} = \mu_f \nabla \boldsymbol{u}_f$, generated by an impeller is another essential parameter for solid suspension in the viscous regime. Figure 7 shows the shear stress distribution at the bottom of the vessel in the zone where particles would tend to settle during normal operation and where all particles are at the beginning of a solid-liquid mixing experiment.

In terms of intensity, the PBT and the ribbon impellers generate low shear stresses compared with the other impellers. For the PBT impeller this can mainly be explained by a larger off-bottom clearance. The Maxblend impeller generates the most important shear stress over a larger zone at the bottom of the tank.

4. Solid-liquid mixing

After investigating the behavior of each impeller in single-phase mixing, we analyze solid-liquid mixing based on the minimum agitation speed required to suspend the particles, the cloud height and the distribution of the particles in the vessel.

4.1. System description

For the solid-liquid mixing simulations the same geometrical parameters (see Table 3) were used. The physical and numerical parameters used in the CFD-DEM model are de-

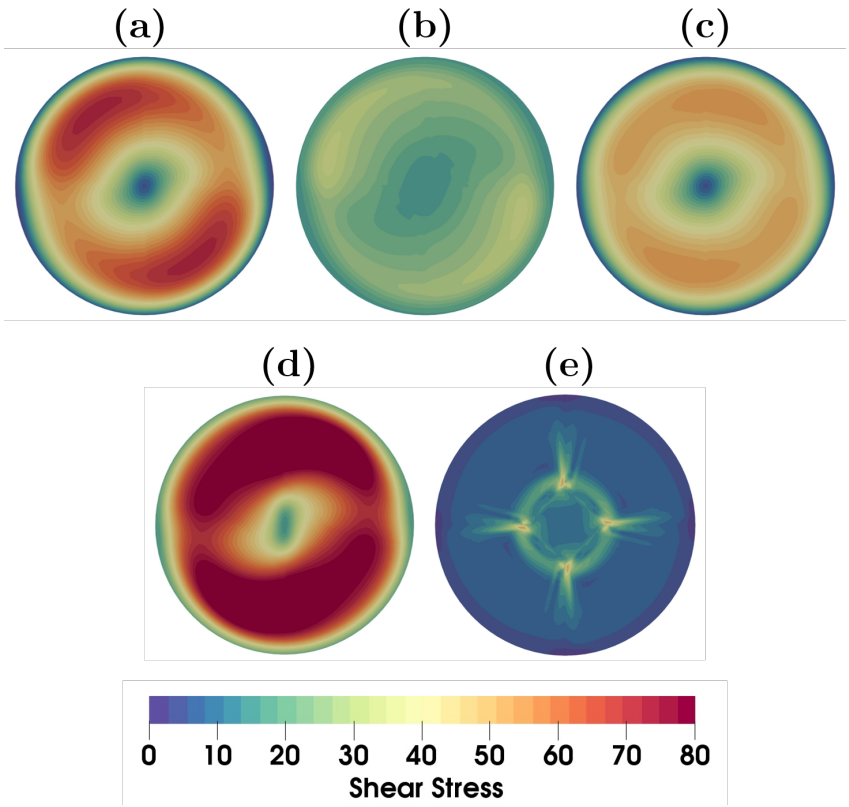

Figure 7: Visualization of the shear stresses at the bottom of the vessels ($z = 0.002cm$) generated by five single-phase mixing systems with the (a) anchor, (b) double helical ribbon, (c) Paravisc, (d) Maxblend, and (e) PBT impellers at a constant Reynolds number of Re=240.

scribed in Table 6 and are the same as in previous numerical and experimental studies [48, 15, 18]. Note that no impeller is in contact with the particle bed at t=0.

Parameter	Symbol	Value
Young's Modulus	Y	100 MPa
Cofficient of restitution	e_r	0.9
Poisson's ratio	ν	0.25
Coefficient of friction	μ_s	0.3
Rolling friction	μ_r	0.1
DEM time step	Δt_{DEM}	5×10^{-6}s
CFD time step	Δt_{CFD}	5×10^{-5}s
Coupling time step	Δt_c	5×10^{-5}s
Particle diameter	d_p	3 mm
Particle density	ρ_p	2500 kg/m^3
Volume fraction	X_v	5.5% (148700 particles)
Fluid density	ρ_f	1390 kg/m^3
Pure fluid viscosity	μ_0	1 Pa.s

Table 6: CFD-DEM simulation parameters and physical properties.

4.2. Minimum agitation speed: N_{js}

The suspended fraction curves for the different impellers (Figure 8) were measured numerically using the Lagrangian suspension fraction analysis method (LSFA). This method considers a particle as suspended if it moves a certain distance Δz_{js} in the axial direction for a certain time Δt_{js} [48].

There is a very similar evolution, and complete suspension is reached for agitation speeds of 100RPM, for the anchor, Paravisc and Maxblend impellers (Figure 8 (a)). For the ribbon and the PBT impellers, complete suspension requires much higher speeds. We estimate an N_{js} of approximately 200RPM for the ribbon impeller and approximately 425RPM for the PBT impeller. The PBT, anchor, Paravisc, and Maxblend impellers displayed comparable performance in terms of power consumption (Figure 8 (b)). However, the double helical ribbon impeller requires more power to completely suspend the particles. This difference was to be expected given the fact that the ribbon impller is the close-clearance impeller that generates the less shear stress (Section 3.5). This confirms the conclusions of the numerical and experimental studies by Blais *et al.* [48, 18] and Lassaigne *et al.* [15], which highlighted the principle of particle bed erosion for the suspension of particles in viscous fluids. To

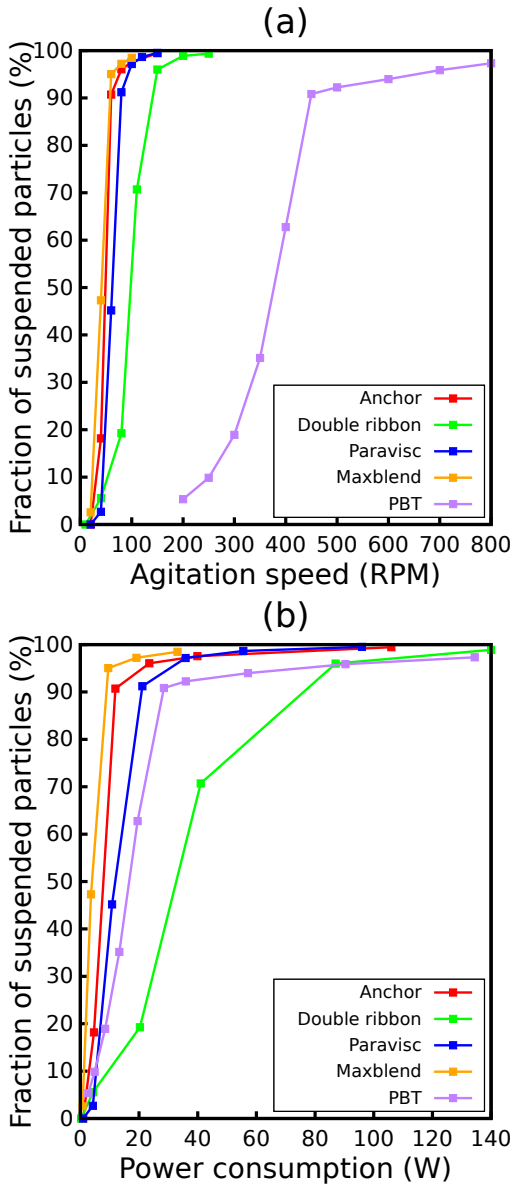

Figure 8: Evolution of the suspended fraction of particles with (a) agitation speed (b) power consumption. The LSFA method was used with the following criteria to measure the suspended fraction: $\Delta z_{js} = d_p$ and $\Delta t_{js} = 2sec$.

summarize, Figure 8 (b) shows that, for close-clearance impellers, the greater the shear stress generated, the lower the power required to suspend the particles.

4.3. Qualitative investigation of the solid-liquid mixing dynamics

Once the minimum agitation speed to completely suspend particles for the different studied system has been estimated we qualitatively analyze the suspension dynamics. It should be noted that the Stokes number gives an indication of the capacity of a particle to deviate from the streamlines of the flow. It can be defined as the ratio between the kinetic energy of the particle and the energy dissipated by friction with the fluid (Eq.15).

$$St = \frac{\rho_p d_p^2 \left|\boldsymbol{u}_f\right|}{18\mu_f T} \tag{15}$$

The different Stokes number profiles for the five systems for agitation speeds equal to N_{js} are compared in Figure 9.

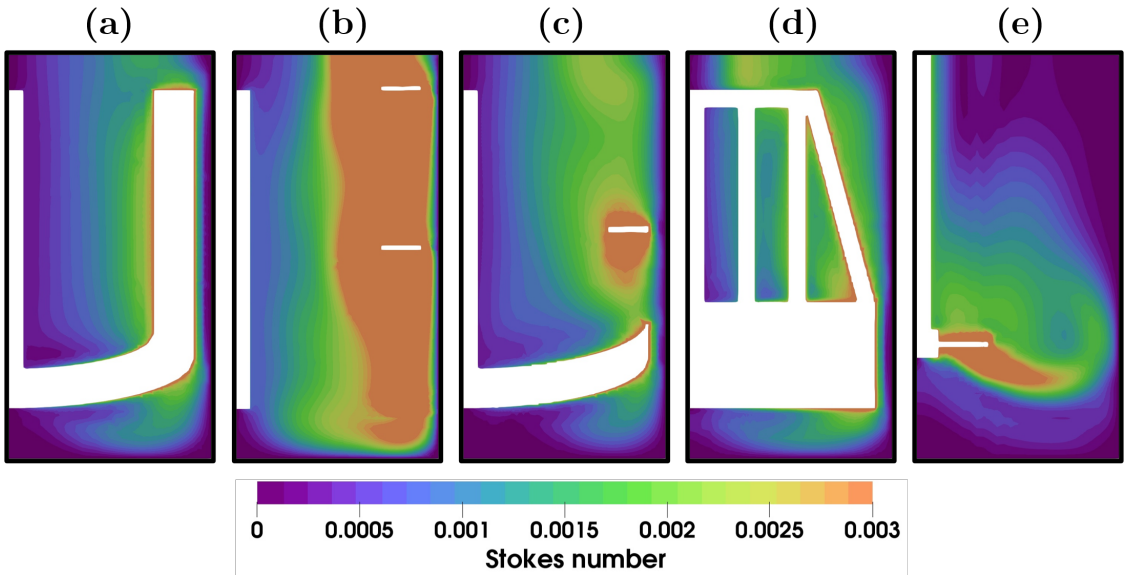

Figure 9: Stokes number profiles at an agitation speed equal to N_{js} for systems with an (a) anchor, (b) double helical ribbon, (c) Paravisc, (d) Maxblend, and (e) PBT impeller.

From this comparison we conclude that particles tend to follow the overall flow of the fluid since all values, in all the volume, remain well below 1.0, the threshold to expect

deviations from the streamlines. We thus rely on single-phase velocity profiles (Section 3.3) to investigate the mixing dynamics. We start by analyzing the void fraction profiles for the different agitation speeds. The results are shown in Figure 10 for the close-clearance impellers and in Figure 11 for the PBT impeller.

- For the anchor impeller, the single-phase study revealed a radial flow that splits into two large recirculating streams. The same behavior is observed for particle motion (Figure 10 (a)). At low speeds, suspension is entirely controlled by the lower recirculation loop, which is clearly visible due the appearance of a toroidal zone of low particle concentration in this zone. These major recirculation zones leads to the suspension of most of the particles, as shown by the evolution of the particle bed at the bottom of the vessel. However, one of the consequences of this double flow is that the particles remain trapped at the bottom of the vessel, considerably limiting the cloud height. It is only at higher velocities that a transition between the upper and lower recirculation loops is initiated.

- With the Maxblend impeller (Figure 10 (d)), the same tendency is observed. The particles follow the flow of the fluid and accumulate along the axis at low agitation speeds, and rise along the wall at higher agitation speeds which coincides perfectly with the shape of the previously mentioned recirculation loops. A better particle distribution is observed in the entire vessel compared with the anchor impeller.

- For the ribbon impeller, the single-phase study showed a strong upward flow along the central axis, indicating that the particles are preferentially suspended along the shaft (Figure 10 (b)). This results in an accumulation of particles in this zone. In addition, there are zones of low particle concentrations around the ribbons, which can be explained by the recirculation loops in the flow patterns. However, as with the Maxblend impeller, relatively good distribution of the particles is possible at higher agitation speeds.

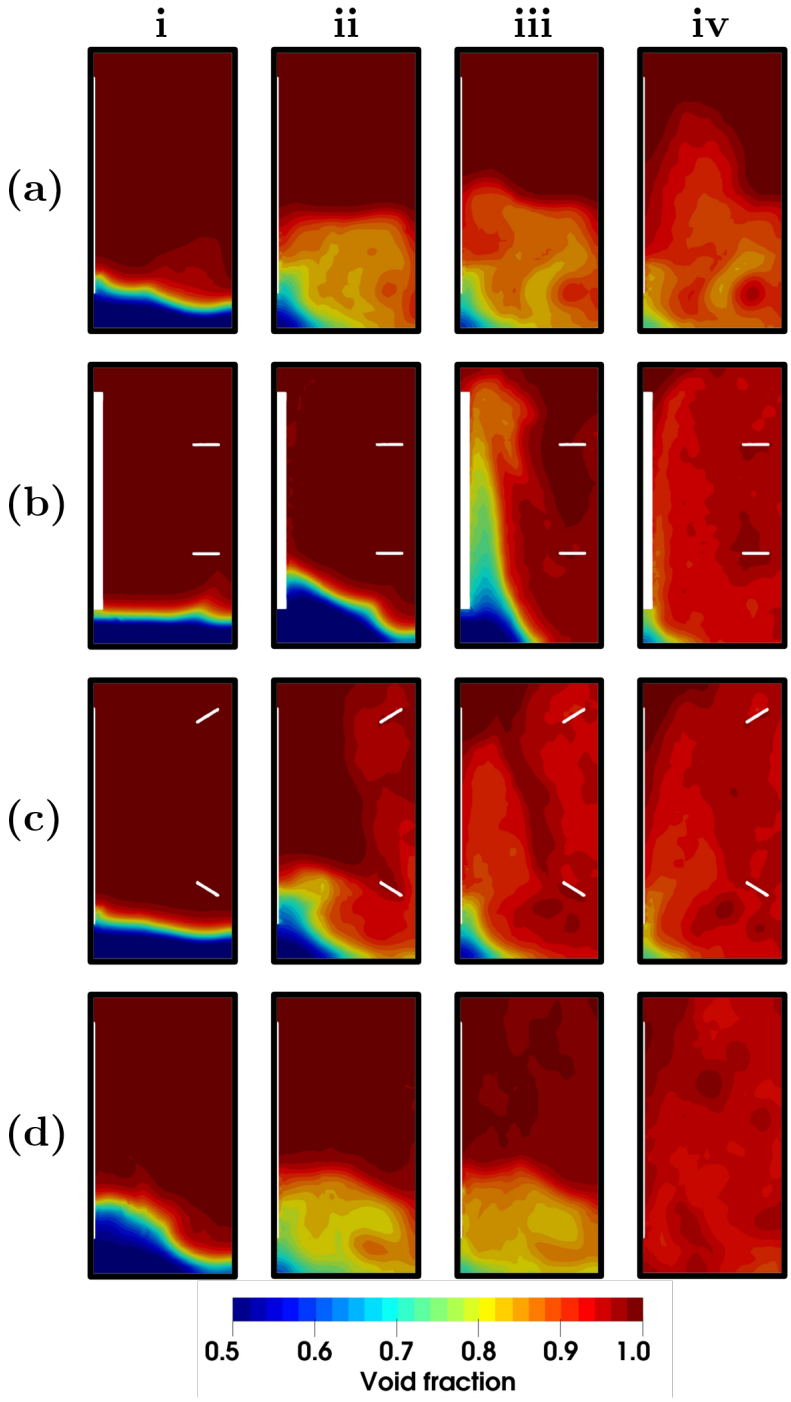

Figure 10: Void fraction profile with the (a) anchor (b) double helical ribbon (c) Paravisc and, (d) Maxblend impellers at different agitation speeds (i) N=40 RPM, (ii) N=80RPM, (iii) N=N_{js} and, (iv) N=150RPM. The agitation speeds (b) (iii) and (iv) for the double helical ribbon impeller are N=150RPM and N=N_{js}=200RPM. These results are presented when the pseudo steady-state is reached.

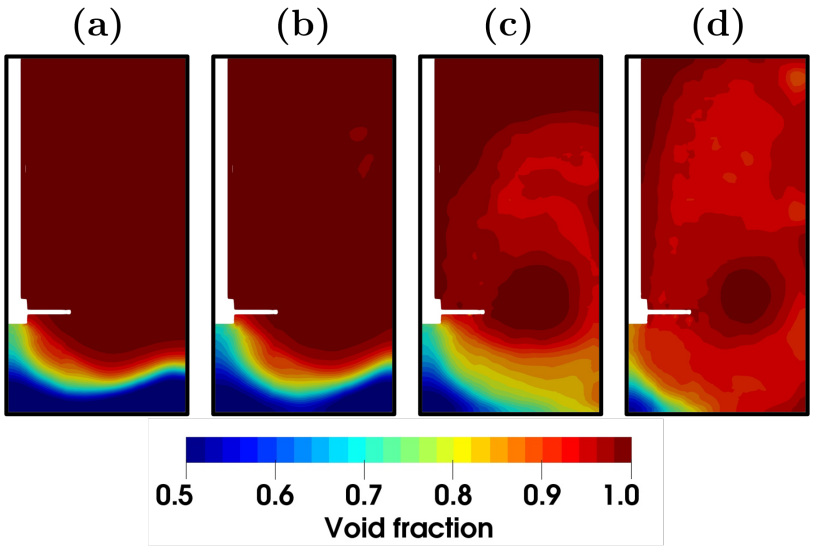

Figure 11: Void-fraction profile with a PBT impeller for (a) $N = 250RPM$, (b) $N = 350RPM$, (c) $N = N_{js} = 425RPM$, (d) $N = 700RPM$, when the pseudo steady-state is reached (adapted from [43]).

– For the Paravisc impeller, we observed a significant axial flow along the walls. This is the zone where the particles are preferentially lifted at the lowest agitation speed (Figure 10 (c)). At higher agitation speeds, the particles are also suspended by a second flow along the central axis, giving a good distribution throughout the entire vessel. However, there is still a small area of low particle concentration in the lower region, which is again the result of the recirculation loop in the flow patterns.

– Lastly, after investigating the behaviors of the close-clearance impellers we compared them with the results obtained for the PBT impeller [15, 18]. This impeller allows global circulation throughout the entire vessel, leading to a good distribution of the particles. However, as is clearly visible in Figure 11, one of the main limitations of this impeller is the large accumulation of particles directly below the shaft and a large zone with a low concentration of particles close to the blades, which is a direct consequence of the flow patterns mentioned in Section 3.3.

To summarize, it is important to generate a strong shear stress to suspend particles. However, this is not enough to obtain a homogeneous suspension, as shown by the profiles

observed with the anchor impeller. In the laminar regime, the fluid must also circulate continuously throughout the entire vessel. Recirculation zones can help homogenize the system, as shown by the profiles observed with the Paravisc and ribbon impellers. However, if these recirculation zones are too large, as is the case for the PBT impeller, this can lead to large areas with low concentrations of particles, which can be detrimental to the quality of the suspension. This preliminary analysis results in a better understanding of the challenges and difficulties related to solid-liquid mixing in the laminar regime. These results are next analyzed quantitatively.

4.4. Quantitative characterization of the solid-liquid mixing systems

This quantitative analysis is broken down into two parts: the cloud height and the local distribution of the particles in the entire vessel.

4.4.1. Cloud height

We start by studying the height reached by the suspensions for each system. Cloud height is an essential parameter for characterizing solid-liquid mixing operations because it reflects the quality of the suspension. Cloud height is defined as the distance from the bottom of the vessel to the level where the majority of the particles are suspended [6]. In our case we used the highest 1478 particles (corresponding to 1% of the particles) and averaged their heights when the pseudo steady-state is reached. The results obtained for each system and different agitation speeds are presented in Figure 12.

As expected, the comparison shows that the anchor impeller is the least effective in terms of cloud height while the Paravisc and Maxblend impellers are the most effective at achieving a high cloud height with lower power consumption. The PBT and double helical ribbon impellers require more power to obtain a cloud height similar to that of the Paravisc and Maxblend impellers.

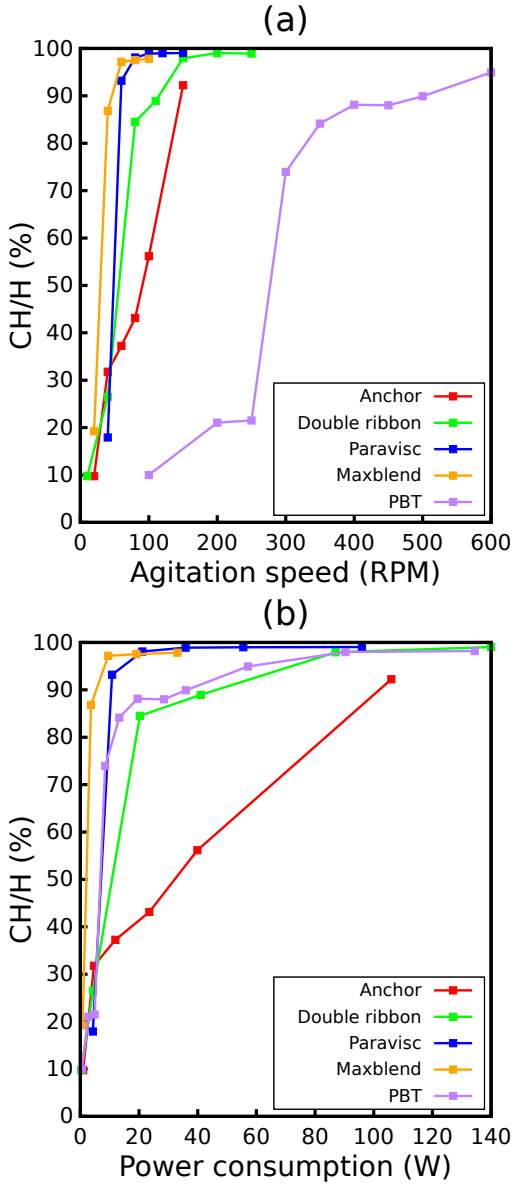

Figure 12: Evolution of cloud height as a function of (a) agitation speed (b) power consumption.

4.4.2. Quantitative distribution of the particles

Section 4.3 revealed that good homogeneity can be achieved with the different impellers. In this section, we compare the power required to achieve a well-mixed state for each configuration. We temporally follow the volume averaged fraction of particles in different regions of the vessel. The vessel is divided into 24 compartments, with a decomposition in three parts along the height, a splitting of the radius in two parts, and a circular decomposition in four parts. To quantify the extent of solid dispersion, we use the RSD approach introduced by Bohnet and Niesmak [73], which is defined as:

$$RSD = \sqrt{\frac{1}{n_c}\sum_{i=1}^{n_c}\left(\frac{X_{v,i}}{X_{v,avg}} - 1\right)^2} \tag{16}$$

where n_c is the number of compartments, $X_{v,i}$ is the particle volume fraction in compartment i and $X_{v,avg}$ is the average volume fraction in the entire vessel. The lower the RSD value, the more uniform the mixing. The initial RSD value ($RSD_{initial}$), with the initial loading, is equal to 2.25 in all cases.

The RSD results shown in Figure 13 correspond to the values obtained when the pseudo-steady state is reached and the values no longer changed. These results confirm that the anchor impeller is the least suitable impeller for efficient mixing with such a system. For the ribbon impeller the power required to obtain good uniformity is relatively high, which prevents it from being competitive. However, its performance in terms of homogeneity is comparable to that of the PBT impeller. Based on this analysis, we conclude that the Paravisc and Maxblend impellers are the most suitable close-clearance impellers for obtaining a homogeneous solid-liquid mixture. For these two better-performing geometries, the one adopted here for the Paravisc is very representative of the ones encountered in the industry. For the Maxblend however, the off-bottom clearance used here is notably larger than what would be found in the industry. With a smaller off-bottom clearance, the suspension performance is expected to improve, which clearly makes this impeller a most suitable geometry

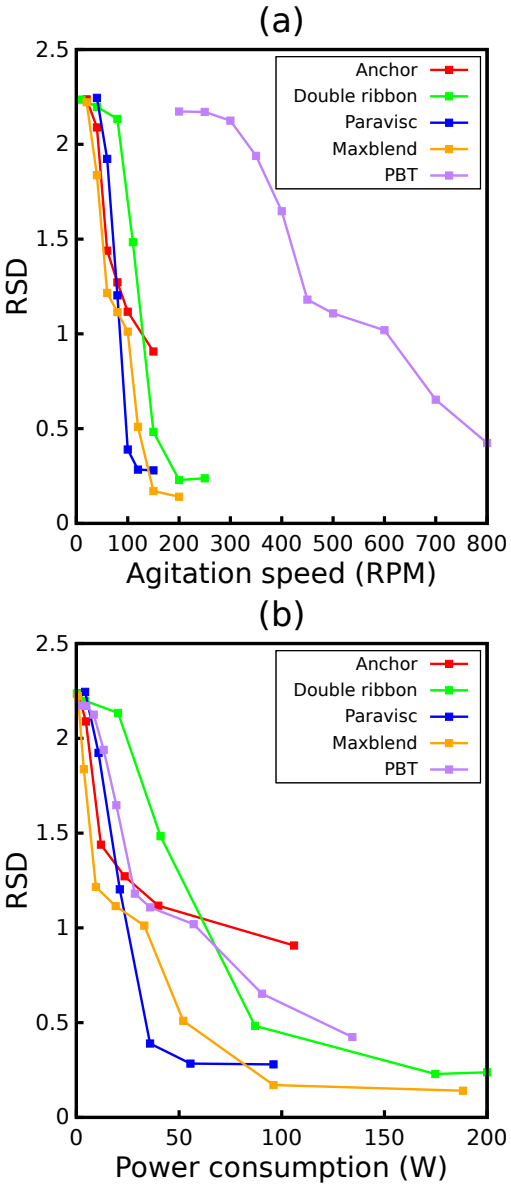

Figure 13: Particle dispersion in the entire mixing vessel at steady state as a function of (a) agitation speed (b) power consumption.

for solid-liquid mixing applications in the laminar regime.

More generally this solid-liquid study for a pure fluid viscosity of μ_0=1Pa.s showed that for close-clearance impellers to achieve an efficient and qualitative suspension, they need to generate a sufficient shear stress to facilitate the onset of the suspension process and to generate a bulk flow that puts the fluid in motion throughout the vessel. It appears from our results that the Paravisc and Maxblend impellers are the most suitable close-clearance impellers for this kind of application. In addition, this comparison shows that impellers with a completely different mixing dynamics, such as the PBT impeller, can give similar or better results than typical close-clearance impellers such as the helical ribbon and anchor.

5. Evaluation of the impact of fluid viscosity

Following the analysis of solid-liquid mixing in the laminar regime, we now investigate the evolution of the behavior of the different impellers when the viscosity is increased. We only use three impeller geometries for this analysis because of their characteristic flows. We no longer consider the anchor impeller due to the poor results obtained with it. We also excluded the Maxblend impeller because its characteristics are very similar to those of the Paravisc impeller, i.e. high shear stress and a large swept volume with an important vertical flow. This study is performed with a pure fluid viscosity of μ_0=4Pa.s, with Reynolds numbers ranging from 20 to 100. The results are given in Figure 14.

In the case of the close-clearance impellers the results are very similar to those of the previous analysis, i.e., it is important to use an impeller that combines good vertical circulation and high shear stress. This is why the Paravisc impeller is preferable to the double helical ribbon impeller. In addition, the PBT impeller produced good results at 1Pa.s but the quality of the suspension degraded with an increase of the viscosity, as shown by the cloud height analysis (Figure 14 (b)). Consequently, the higher the viscosity the more close-clearance impellers such as the Paravisc outperforms other impellers in terms of efficient solid-liquid mixing. Such an observation probably explains why dual-shaft mixers, combin-

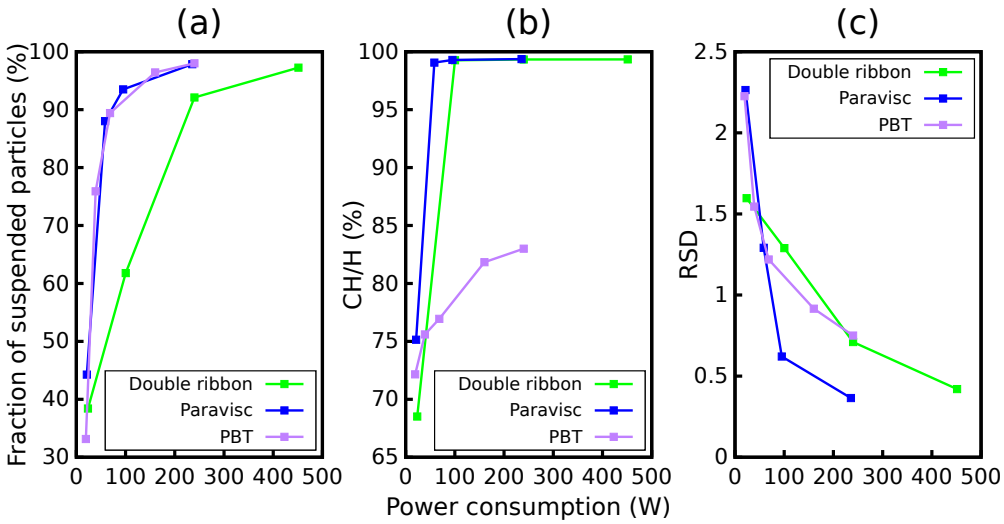

Figure 14: Evolution of the (a) fraction of suspended particles, (b) cloud height, and (c) particle dispersion, as a function of power consumption for the three impellers, with a pure dynamic viscosity of μ_0=4Pa.s.

ing PBT and a close-clearance impeller, have been designed to cope with extremely complex multiphase fluids such as those in the cosmetic, paints and adhesive industries.

6. Conclusion

Despite numerous applications, solid-liquid mixing has been studied much less in the laminar regime than in the turbulent regime. However, experimental studies showed that the learnings obtained in the turbulent regime are different from those obtained in the laminar regime. This is why it is important to develop new tools to study more specifically solid-liquid mixing in the laminar regime. In a previous work, we developped an unresolved CFD-DEM model in a rotating frame of reference that is based on the CFDEM framework. This model has several advantages for studying solid-liquid mixing in a viscous regime. The fact that it is based on a rotating frame of reference makes it possible to study any symmetrical impeller geometry, particularly close-clearance impellers. The CFD-DEM approach also provides a highly accurate description of granular dynamics because the movement of each particle is modeled individually through DEM. This aspect is particularly interesting for the analysis of the suspended fractions, cloud heights, and homogeneities of mixing systems.

The objective of the present study was to use this CFD-DEM model to study the solid-liquid mixing performance of close-clearance impellers that display good efficiency for single-phase viscous mixing operations. We focused on four close-clearance impeller geometries: the anchor, double helical ribbon, Paravisc, and Maxblend. They were compared with the PBT, a more commonly used and widely studied impeller.

We shed light on the different mechanisms involved in the suspension of particles in a viscous fluid. First, the onset of suspension is controlled by an erosion mechanism. Thus, the higher the shear stress generated by the impeller, the easier the suspension. This explains why a lower suspension speed N_{js} was obtained with the anchor, Paravisc, and Maxblend impellers. Once in suspension, the particle motion is mainly controlled by the bulk of the flow. Impellers that only generate shear stress without global pumping are thus not ideal for distributing particles throughout the entire vessel. This is also why the anchor impeller generates suspensions with a low cloud height and a non-uniform distribution of particles. However, in the case of the double ribbon, Paravisc, and Maxblend impellers, the circulation of the liquid distributes the particles more uniformly. In terms of energy efficiency, the double ribbon impeller is less efficient than the Paravisc and Maxblend impellers. This can be explained by the difference in the amount of shear stress generated.

We compared the performances of the close-clearance impellers with that of the PBT impeller and concluded that the use of the PBT is justified, to a certain extent, in the laminar regime. For a Reynolds number of 200 it performs better than the double helical ribbon and anchor impellers and slightly worse than the Paravisc and Maxblend impellers. However, the closer the regime is to the creeping flow, the better the close-clearance impellers performed.

In a nutshell, the best impeller for achieving efficient solid-liquid mixing in the laminar regime is one that generates high shear stress and strong bulk flow in the entire vessel. Given this, it would be preferable to use close-clearance impellers such as the Paravisc and the Maxblend. This is especially true at larger pure fluid viscosities.

7. Acknowledgements

The financial support from the Natural Sciences and Engineering Research Council of Canada (NSERC) is gratefully acknowledged. Computations were made on supercomputers Cedar and Graham managed by Compute Canada. In particular, the authors would like to acknowledge the efficient support received from Calcul Québec and Compute Canada systems analysts.

References

[1] M. Zlokarnik, Stirring: Theory and Practice, John Wiley & Sons, 2008.

[2] E. L. Paul, V. A. Atiemo-Obeng, S. M. Kresta, Handbook of Industrial Mixing: Science and Practice, John Wiley & Sons, 2004.

[3] F. Kneule, Die prüfung von rührern durch löslichkeitsbestimmung, Chemie Ingenieur Technik 28 (3) (1956) 221–225.

[4] F. S. Hirsekorn, S. A. Miller, Agitation of viscous solid-liquid suspensions, Chemical Engineering Progress 49 (9) (1953) 459–466.

[5] T. N. Zwietering, Suspending of solid particles in liquid by agitators, Chemical Engineering Science 8 (3) (1958) 244–253. doi:10.1016/0009-2509(58)85031-9.

[6] V. A. Atiemo-Obeng, W. R. Penney, P. Armenante, Solid-liquid mixing, Handbook of industrial mixing: Science and practice (2004) 543–584.

[7] A. Nienow, Suspension of solid particles in turbine agitated baffled vessels, Chemical Engineering Science 23 (12) (1968) 1453–1459. doi:10.1016/0009-2509(68)89055-4.

[8] G. Baldi, R. Conti, E. Alaria, Complete suspension of particles in mechanically agitated vessels, Chemical Engineering Science 33 (1) (1978) 21–25.

[9] P. Armenante, E. Nagamine, J. Susanto, Determination of correlations to predict the minimum agitation speed for complete solid suspension in agitated vessels, Canadian Journal of Chemical Engineering 76 (3) (1998) 413–419.

[10] I. Ayranci, T. Ng, A. W. Etchells, S. M. Kresta, Prediction of just suspended speed for mixed slurries at high solids loadings, Chemical Engineering Research and Design 91 (2) (2013) 227–233. doi:10.1016/j.cherd.2012.08.002.

[11] A. Tamburini, A. Brucato, A. Busciglio, A. Cipollina, F. Grisafi, G. Micale, F. Scargiali, G. Vella, Solid-Liquid Suspensions in Top-Covered Unbaffled Vessels: Influence of Particle Size, Liquid Viscosity, Impeller Size, and Clearance, Ind. Eng. Chem. Res. 53 (23) (2014) 9587–9599. doi:10.1021/ie500203r.

[12] R. Grenville, J. Giacomelli, D. Brown, Suspension of solid particles in vessels agitated by Rushton turbine imperllers, Chemical Engineering Research and Design 109 (2016) 730–733. doi:10.1016/j.cherd.2016.03.024.

[13] C. E. Choong, S. Ibrahim, A. El-Shafie, Artificial Neural Network (ANN) model development for predicting just suspension speed in solid-liquid mixing system, Flow Measurement and Instrumentation (2020) 101689.

[14] I. Ayranci, S. M. Kresta, Critical analysis of Zwietering correlation for solids suspension in stirred tanks, Chemical Engineering Research and Design 92 (3) (2014) 413–422. doi:10.1016/j.cherd.2013.09.005.

[15] M. Lassaigne, B. Blais, L. Fradette, F. Bertrand, Experimental investigation of the mixing of viscous liquids and non-dilute concentrations of particles in a stirred tank, Chemical Engineering Research and Design 108 (2016) 55–68. doi:10.1016/j.cherd.2016.01.005.

[16] S. Ibrahim, A. Nienow, Comparing Impeller Performance for Solid-Suspension in the

Transitional Flow Regime with Newtonian Fluids, Chemical Engineering Research and Design 77 (8) (1999) 721–727. doi:10.1205/026387699526863.

[17] S. Hosseini, D. Patel, F. Ein-Mozaffari, M. Mehrvar, Study of solid- liquid mixing in agitated tanks through computational fluid dynamics modeling, Industrial & Engineering Chemistry Research 49 (9) (2010) 4426–4435.

[18] B. Blais, F. Bertrand, CFD-DEM investigation of viscous solid–liquid mixing: Impact of particle properties and mixer characteristics, Chemical Engineering Research and Design 118 (2017) 270–285. doi:10.1016/j.cherd.2016.12.018.

[19] M. T. Hicks, K. J. Myers, A. Bakker, Cloud height in solids suspension agitation, Chemical Engineering Communications 160 (1) (1997) 137–155.

[20] P. Mishra, F. Ein-Mozaffari, Using computational fluid dynamics to analyze the performance of the Maxblend impeller in solid-liquid mixing operations, International Journal of Multiphase Flow 91 (2017) 194–207.

[21] R. K. Grenville, A. T. C. Mak, D. A. R. Brown, Suspension of solid particles in vessels agitated by axial flow impellers, Chemical Engineering Research and Design 100 (2015) 282–291.

[22] B. Blais, O. Bertrand, L. Fradette, F. Bertrand, CFD-DEM simulations of early turbulent solid–liquid mixing: Prediction of suspension curve and just-suspended speed, Chemical Engineering Research and Design 123 (2017) 388–406.

[23] A. Tamburini, A. Cipollina, G. Micale, A. Brucato, M. Ciofalo, CFD simulations of dense solid–liquid suspensions in baffled stirred tanks: Prediction of suspension curves, Chemical Engineering Journal 178 (2011) 324–341.

[24] A. Tamburini, A. Cipollina, G. Micale, A. Brucato, M. Ciofalo, CFD simulations of

dense solid–liquid suspensions in baffled stirred tanks: Prediction of the minimum impeller speed for complete suspension, Chemical engineering journal 193 (2012) 234–255.

[25] J. de la Villéon, F. Bertrand, P. A. Tanguy, R. Labrie, J. Bousquet, D. Lebouvier, Numerical investigation of mixing efficiency of helical ribbons, AIChE Journal 44 (4) (1998) 972–977. doi:10.1002/aic.690440423.

[26] A. Bakker, L. E. Gates, Properly choose mechanical agitators for viscous liquids, Chem. Eng. Prog. 91 (12) (1995) 25–34.

[27] P. A. Tanguy, F. Thibault, E. B. De La Fuente, A new investigation of the metzner-otto concept for anchor mixing impellers, The Canadian Journal of Chemical Engineering 74 (2) (1996) 222–228.

[28] D. C. Peters, J. M. Smith, Mixing in anchor agitated vessels, The Canadian Journal of Chemical Engineering 47 (3) (1969) 268–271.

[29] J. Sawinsky, G. Havas, A. Deak, Power requirement of anchor and helical ribbon impellers for the case of agitating Newtonian and pseudo-plastic liquids, Chemical Engineering Science 31 (6) (1976) 507–509.

[30] G. Delaplace, J.-C. Leuliet, G. Ronse, Power requirement when mixing a shear-thickening fluid with a helical ribbon impeller type, Chemical Engineering & Technology: Industrial Chemistry-Plant Equipment-Process Engineering-Biotechnology 23 (4) (2000) 329–335.

[31] A. R. Khopkar, L. Fradette, P. A. Tanguy, Hydrodynamics of a dual shaft mixer with Newtonian and non-Newtonian fluids, Chemical Engineering Research and Design 85 (6) (2007) 863–871.

[32] W. Yao, M. Mishima, K. Takahashi, Numerical investigation on dispersive mixing char-

acteristics of Maxblend and double helical ribbons, Chemical Engineering Journal 84 (3) (2001) 565–571.

[33] C. Devals, M. Heniche, K. Takenaka, P. A. Tanguy, CFD analysis of several design parameters affecting the performance of the Maxblend impeller, Computers & Chemical Engineering 32 (8) (2008) 1831–1841. doi:10.1016/j.compchemeng.2007.09.007.

[34] S. B. Pour, L. Fradette, P. A. Tanguy, Laminar and slurry blending characteristics of a dual shaft impeller system, Chemical Engineering Research and Design 85 (9) (2007) 1305–1313.

[35] O. Bertrand, B. Blais, F. Bertrand, L. Fradette, Complementary methods for the determination of the just-suspended speed and suspension state in a viscous solid–liquid mixing system, Chemical Engineering Research and Design 136 (2018) 32–40. doi:10.1016/j.cherd.2018.04.035.

[36] L. Fradette, P. A. Tanguy, F. Bertrand, F. Thibault, J.-B. Ritz, E. Giraud, CFD phenomenological model of solid–liquid mixing in stirred vessels, Computers & Chemical Engineering 31 (4) (2007) 334–345. doi:10.1016/j.compchemeng.2006.07.013.

[37] G. Micale, G. Montante, F. Grisafi, A. Brucato, J. Godfrey, CFD simulation of particle distribution in stirred vessels, Chemical Engineering Research and Design 78 (3) (2000) 435–444.

[38] M. Ljungqvist, A. Rasmuson, Numerical simulation of the two-phase flow in an axially stirred vessel, Chemical Engineering Research and Design 79 (5) (2001) 533–546.

[39] A. Tamburini, A. Cipollina, G. Micale, A. Brucato, M. Ciofalo, CFD simulations of dense solid–liquid suspensions in baffled stirred tanks: Prediction of solid particle distribution, Chemical engineering journal 223 (2013) 875–890.

[40] G. Montante, K. Lee, A. Brucato, M. Yianneskis, Numerical simulations of the dependency of flow pattern on impeller clearance in stirred vessels, Chemical Engineering Science 56 (12) (2001) 3751–3770.

[41] G. Micale, F. Grisafi, L. Rizzuti, A. Brucato, CFD simulation of particle suspension height in stirred vessels, Chemical Engineering Research and Design 82 (9) (2004) 1204–1213.

[42] B. Blais, M. Lassaigne, C. Goniva, L. Fradette, F. Bertrand, A semi-implicit immersed boundary method and its application to viscous mixing, Computers & Chemical Engineering 85 (2016) 136–146. doi:10.1016/j.compchemeng.2015.10.019.

[43] B. Delacroix, J. Rastoueix, L. Fradette, F. Bertrand, B. Blais, CFD-DEM simulations of solid-liquid flow in stirred tanks using a non-inertial frame of reference, Chemical Engineering Science (2020) 116137.

[44] B. Delacroix, A. Bouarab, L. Fradette, F. Bertrand, B. Blais, Simulation of granular flow in a rotating frame of reference using the discrete element method, Powder Technology 369 (2020) 146–161. doi:10.1016/j.powtec.2020.05.006.

[45] CFDEM, CFDEM-Opensource CFD, DEM and CFD–DEM, https://www.cfdem.com/ (2020).

[46] LIGGGHTS. (2011). LAMMPS improved for general granular and granular heat transfer simulations. Retrieved from http://www.liggghts.com.

[47] OpenCFD, OpenFOAM – the opensource CFD toolbox, https://www.openfoam.com/ (2020).

[48] B. Blais, M. Lassaigne, C. Goniva, L. Fradette, F. Bertrand, Development of an unresolved CFD–DEM model for the flow of viscous suspensions and its applica-

tion to solid–liquid mixing, Journal of Computational Physics 318 (2016) 201–221. doi:10.1016/j.jcp.2016.05.008.

[49] H. P. Zhu, Z. Y. Zhou, R. Y. Yang, A. B. Yu, Discrete particle simulation of particulate systems: A review of major applications and findings, Chemical Engineering Science 63 (23) (2008) 5728–5770. doi:10.1016/j.ces.2008.08.006.

[50] B. Blais, D. Vidal, F. Bertrand, G. S. Patience, J. Chaouki, Experimental Methods in Chemical Engineering: Discrete Element Method—DEM, The Canadian Journal of Chemical Engineering 97 (7) (2019) 1964–1973. doi:10.1002/cjce.23501.

[51] B.Delacroix, A.Bouarab, L.Fradette, F.Bertrand, B.Blais, Simulation of granular flow in a rotating frame of reference using the Discrete Element Method, Submitted to Powder Technology Journal (2020).

[52] H. P. Zhu, Z. Y. Zhou, R. Y. Yang, A. B. Yu, Discrete particle simulation of particulate systems: Theoretical developments, Chemical Engineering Science 62 (13) (2007) 3378–3396. doi:10.1016/j.ces.2006.12.089.

[53] Y. Tsuji, T. Tanaka, T. Ishida, Lagrangian numerical simulation of plug flow of cohesionless particles in a horizontal pipe, Powder Technology 71 (3) (1992) 239–250. doi:10.1016/0032-5910(92)88030-L.

[54] K. L. JOHNSON, Normal contact of elastic solids : Hertz theory, Contact Mechanics (1989) 84–106.

[55] R. D. MINDLIN, Elastic Spheres in Contact Under Varying Oblique Forces, J. Applied Mech. 20 (1953) 327–344.

[56] C. T. Crowe, J. D. Schwarzkopf, M. Sommerfeld, Y. Tsuji, J. D. Schwarzkopf, M. Sommerfeld, Y. Tsuji, Multiphase Flows with Droplets and Particles, CRC Press, 2011. doi:10.1201/b11103.

[57] R. I. Issa, Solution of the implicitly discretised fluid flow equations by operator-splitting, Journal of computational physics 62 (1) (1986) 40–65.

[58] G. K. Batchelor, J. T. Green, The determination of the bulk stress in a suspension of spherical particles to order c 2, Journal of Fluid Mechanics 56 (3) (1972) 401–427.

[59] I. M. Krieger, T. J. Dougherty, A mechanism for non-Newtonian flow in suspensions of rigid spheres, Transactions of the Society of Rheology 3 (1) (1959) 137–152.

[60] H. A. Barnes, J. F. Hutton, K. Walters, An Introduction to Rheology, Elsevier, 1989.

[61] S. Pirker, D. Kahrimanovic, C. Goniva, Improving the applicability of discrete phase simulations by smoothening their exchange fields, Applied Mathematical Modelling 35 (5) (2011) 2479–2488. doi:10.1016/j.apm.2010.11.066.

[62] P. Mishra, F. Ein-Mozaffari, Critical review of different aspects of liquid-solid mixing operations, Reviews in Chemical Engineering 0 (0) (2019). doi:10.1515/revce-2018-0017.

[63] D. Gu, Z. Liu, F. Qiu, J. Li, C. Tao, Y. Wang, Design of impeller blades for efficient homogeneity of solid-liquid suspension in a stirred tank reactor, Advanced Powder Technology 28 (10) (2017) 2514–2523. doi:10.1016/j.apt.2017.06.027.

[64] J. J. Derksen, Numerical simulation of solids suspension in a stirred tank, AIChE Journal 49 (11) (2003) 2700–2714.

[65] R. Di Felice, The voidage function for fluid-particle interaction systems, International Journal of Multiphase Flow 20 (1) (1994) 153–159.

[66] S. V. Patankar, D. B. Spalding, A calculation procedure for heat, mass and momentum transfer in three-dimensional parabolic flows, in: Numerical Prediction of Flow, Heat Transfer, Turbulence and Combustion, Elsevier, 1983, pp. 54–73.

[67] H. Ameur, Y. Kamla, D. Sahel, Performance of helical ribbon and screw impellers for mixing viscous fluids in cylindrical reactors, ChemEngineering 2 (2) (2018) 26.

[68] A. Iranshahi, C. Devals, M. Heniche, L. Fradette, P. A. Tanguy, K. Takenaka, Hydrodynamics characterization of the Maxblend impeller, Chemical Engineering Science 62 (14) (2007) 3641–3653.

[69] C. Rivera, S. Foucault, M. Heniche, T. Espinosa-Solares, P. A. Tanguy, Mixing analysis in a coaxial mixer, Chemical Engineering Science 61 (9) (2006) 2895–2907.

[70] A. Iranshahi, M. Heniche, F. Bertrand, P. A. Tanguy, Numerical investigation of the mixing efficiency of the Ekato Paravisc impeller, Chemical Engineering Science 61 (8) (2006) 2609–2617.

[71] G. Delaplace, R. Guerin, J.-C. Leuliet, R. P. Chhabra, An analytical model for the prediction of power consumption for shear-thinning fluids with helical ribbon and helical screw ribbon impellers, Chemical engineering science 61 (10) (2006) 3250–3259.

[72] G. Delaplace, J. C. Leuliet, V. Relandeau, Circulation and mixing times for helical ribbon impellers. Review and experiments, Experiments in fluids 28 (2) (2000) 170–182.

[73] M. Bohnet, G. Niesmak, Distribution of solids in stirred suspensions, Ger. Chem. Eng 3 (1) (1980) 57–65.